Energy Storage Materials 86 (2026) 104994

Contents lists available at ScienceDirect

Energy Storage Materials

journal homepage: www.elsevier.com/locate/ensm

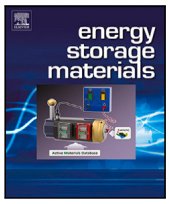

Unraveling inhomogeneous rocksalt growth in Ni-rich cathode materials for Li-ion batteries

Svenja Both [a,b], Simon Hein [a,b], Arnulf Latz [a,b,c], Timo Danner [a,b,*]

[a] German Aerospace Center (DLR), Institute of Engineering Thermodynamics, 89081 Ulm, Germany
[b] Helmholtz-Institute Ulm for Electrochemical Energy Storage (HIU), 89081 Ulm, Germany
[c] Institute of Electrochemistry, Ulm University, 89081 Ulm, Germany

ARTICLE INFO

Keywords:
Li-ion batteries
Ni-rich cathodes
Degradation
Rocksalt
Structure-resolved simulation
Continuum model

ABSTRACT

Ni-rich cathode materials suffer from structural instability when cycled to high cutoff voltages. A transformation from the layered crystal structure to other phases, such as rocksalt, deteriorates the particle surface at low states of lithiation. Inhomogeneous potential and concentration fields as they occur in electrodes can have a significant impact on the degradation. In this work, we demonstrate rocksalt growth on a realistic high-energy NMC811 electrode using 3D microstructure-resolved simulations. We unravel inhomogeneities through transport in the electrode with a stronger active material degradation near the separator. To study individual particles in the electrode, we apply a watershed algorithm to segment the structure into distinct particles. A high correlation between both particle size as well as particle position and rocksalt thickness is observed in our half-cell simulations. We further shed light on inhomogeneities that can arise on single-particle level due to inhomogeneous lithiation.

1. Introduction

Ni-rich cathode materials are promising cathode materials for Li-ion batteries due to their high energy and power density [1]. The achievable capacity for a given cutoff voltage increases with increasing Ni content [2], which makes Ni-rich stoichiometries with 80% of Ni content or higher, such as $Li_xNi_{0.8}Mn_{0.1}Co_{0.1}O_2$ (NMC811) an excellent choice for cathode materials. One major drawback in their application is a severe material instability when cycling to high cutoff voltages [2,3], i.e. low states of lithiation. A transformation of the layered NMC structure to resistive phases, like a rocksalt phase, has been observed experimentally in a highly delithiated state [4–6]. A rocksalt phase hinders Li^+ diffusion in the active material [7], and therefore reduces intercalation kinetics [6–8]. This leads to cathode polarization and a decreased rate capability [9]. Furthermore, a loss of active material due to a lack of intercalation sites results from the transformation [9]. Additionally, the formation of a fatigued phase due to lattice mismatch between the layered and the degraded material has been proposed [4]. The transformation process involves the loss of highly reactive lattice oxygen [2,6,10,11], which can further react with the organic solvents in the electrolyte [10–13]. The mechanism is not limited to Ni-rich cathode materials such as NMC [5] or $LiNiO_2$ [8] in liquid electrolyte systems, but is an important degradation mechanisms in solid-state batteries [14] or Na-ion batteries [15,16] as well. To mitigate oxygen loss and phase transformation, developing surface coatings or doping the active material is an active area of research [17,18]. Furthermore, the rocksalt phase poses a challenge for recycling and up-cycling of spent batteries [19]. Other failure mechanisms include the growth of a cathode electrolyte interphase (CEI) layer [20–22], transition metal dissolution [23–25], particle cracking [26–28] or current collector corrosion [29]. Transition metal dissolution has been found especially at high cut-off-voltages [23,24,30] and could be linked to oxygen loss by follow-up reactions with the electrolyte that produce acidic species [13,30]. Cracks expose fresh surface area, that suffer from rocksalt formation again [28]. CEI and rocksalt formation have been shown to occur simultaneously [13,20]. However, recent work by Vettori et al. [20] proposed rocksalt formation to be the critical degradation mechanism compared to CEI formation. Therefore, it is crucial to understand the causes and impact of rocksalt formation and oxygen loss in Ni-based materials. Experimentally, the resistive phases have been investigated using high-resolution imaging techniques such as transmission electron microscopy (TEM) [5,13,31,32]. Oxygen loss has been characterized using on-line electrochemical mass spectrometry (OEMS) at distinct states-of-lithiation [2,3,13,33], typically around 80 % state of charge (SOC) for Ni-rich materials [2,3].

On an electrode level, Freiberg et al. observed a different onset potentials of oxygen evolution at different current densities, which

* Corresponding author at: German Aerospace Center (DLR), Institute of Engineering Thermodynamics, 89081 Ulm, Germany.
E-mail address: timo.danner@dlr.de (T. Danner).

https://doi.org/10.1016/j.ensm.2026.104994
Received 2 December 2025; Received in revised form 30 January 2026; Accepted 14 February 2026
Available online 17 February 2026

they attributed to concentration inhomogeneities in the electrode [34]. *Operando* imaging via optical scattering microscopy recently revealed inhomogeneous lithiation of single NMC particles due to an inhomogeneous rocksalt layer [35]. However, imaging techniques are inherently limited to a small region of interest, which makes high-resolution studies of degradation challenging for whole electrodes. Especially in thick high-energy electrodes or at high applied currents, e.g. in fast-charging applications, inhomogeneities and transport processes in the electrode can be of great importance.

To shed light on inhomogeneous lithiation and degradation, computational investigations can help in the understanding of such degradation processes. Several studies investigate Ni-rich cathode materials and their degradation with ab-initio simulations using density functional theory and molecular dynamics [36–38]. While this is important for a mechanistic understanding of the transformation process, simulations on the continuum scale are required to resolve transport phenomena on an electrode level. On the continuum scale, cathode degradation has been previously simulated using homogenized P2D-models [39,40] or single particle models [41]. In a previous study, we investigated a commercial Ni-rich electrode using a novel P2D model to simulate rocksalt growth and oxygen release [40]. A strong inhomogeneity across the electrode was predicted, with a thicker rocksalt layer at the separator and a thinner layer at the current collector. A similar trend was observed by Zhuo et al. [39] in their shrinking-core model implemented in PyBAMM. Previous studies on mechanical damage, without modeling degradation, suggested a similar trend with larger damage at the separator and smaller damage at the current collector due to local inhomogeneities in concentration [26,42,43]. Both through- and in-plane heterogeneity in Li-ion concentration have also been observed using structure-resolved simulations [44,45].

While electrochemical simulation tools exist that investigate whole electrodes, spatially resolved rocksalt growth has never been simulated using a real cathode microstructure. Local inhomogeneities in the electrode lead to a variety of local concentrations and current densities, which also affect active material deterioration. The impact of microstructure on degradation phenomena, such as growth of a solid-electrolyte-interphase (SEI) and lithium plating, has been demonstrated using 3D microstructure-resolved simulations [46,47].

To investigate the local degradation of Ni-rich cathode active material, we use structure-resolved electrochemical continuum simulations on a realistic, high-resolution electrode microstructure [48]. By applying a watershed algorithm to the structure, we highlight distinct particles of various sizes and positions to unravel the spatial distribution of rocksalt growth on individual particles. While previous experimental work on individual single-particles revealed an inhomogeneity in phase transformation [35], the interplay between electrode structure and degradation has not been investigated before. Our work unveils inhomogeneities that are caused by the particle size and position in the electrode in addition to inhomogeneities arising on single particles. Due to our 3D microstructure-resolved simulation framework, the investigated particles are embedded in the complex electrode matrix influenced by particle size or CBD distribution. This allows for an investigation of individual particles under realistic concentration and potential fields. Therefore, this study aims to complement and inform experimental observations and guide electrode design, as it offers the possibility to correlate degradation with individual material features and provide insights that are hardly accessible experimentally. Our simulative analysis provides a unique understanding of realistic electrodes and can help to guide further experimental work on the topic.

2. Methods

First, we introduce the microstructure of a commercial NMC811 electrode. We then discuss our continuum modeling approach to describe Li and electron transport in Li-ion batteries and present our aging model for the layered-to-rocksalt transformation. In the last paragraph, technical aspects like particle segmentation using a watershed algorithm on the full electrode structure to study individual particles are introduced.

2.1. Electrode structure and continuum model

We study a realistic, high-energy NMC811 electrode, which was investigated in detail in previous work using high-resolution tomography (focused ion beam-scanning electron microscopy (FIB-SEM)) [48]. Our simulation setup consists of this cathode structure, a homogenized separator and a lithium metal counter electrode as well as a current collector on each side. The setup is shown in the Supporting Information.

In previous work, we presented a novel continuum modeling approach to model phase transformation and oxygen release on this electrode [40]. The model is based on a Doyle–Fuller–Newman (DFN) type of model [49], i.e. following a so-called pseudo-2D (P2D) approach, and was parameterized consistently to predict the phase transformation process on the high-energy electrode from Ref. [48]. In this work, we extend this model formulation from P2D to 3D by incorporating it into our framework for microstructure-resolved simulations BEST [50]. Charge and mass conservation equations for the active material and the electrolyte phase are solved in each voxel of the structure, thus allowing for direct simulation on the FIB-SEM geometry. Conductive additive and binder are treated as a homogenized domain (Carbon-Binder-Domain (CBD)) with effective parameters for electronic and ionic transport. More information on the 3D model can be found in Refs. [50–52] and in the Supporting Information. As shown in previous work [48], the amount and distribution of CBD has a significant impact on the lithiation behavior of the electrode. Therefore, it would be interesting to study the impact of CBD distribution on the local degradation. As our microstructure used for simulation contains CBD, we take into account its effect on the resulting concentration and potential field. However, the effect of CBD coverage on the active material transformation is not understood yet. Therefore, investigating the formation of rocksalt at interfaces between active material and CBD domains needs future work, e.g. atomistic calculations, to understand the formation dynamics.

Our degradation model is applied between active material and electrolyte interfaces. It will be briefly summarized in the following, for a more detailed discussion and explanation the reader is referred to Ref. [40]. The rocksalt thickness equation is based on the general relation between oxygen flux $\vec{j}_{O_2}$ and phase transformation:

$$\frac{dL_{RS}}{dt} = \frac{V_{RS}}{\upsilon_{stoich}} \cdot \vec{j}_{O_2} \cdot \vec{n} \tag{1}$$

with V_{RS} as the molar volume of the rocksalt phase, υ_{stoich} as the stoichiometric coefficient of the transformation reaction and the surface normal $\vec{n}$. The oxygen flux is modeled using Fick's first law of diffusion in one dimension:

$$\vec{j}_{O_2} = D_{ox} \frac{c_{O_2,mob}}{L_{RS}} \tag{2}$$

It is driven by the concentration gradient of mobile oxygen, which evolves at the interface and is assumed to be 0 at the outer particle surface due to instantaneous follow-up reactions with the electrolyte. The concentration of mobile oxygen at the interface is based on oxygen vacancy formation energies $\Delta G(c_{Li})$ as a function of state of lithiation and can be seen in Eq. (3). $\Delta G(c_{Li})$ is assumed to be negative below approximately 22.5% state of lithiation, thus enabling spontaneous vacancy formation below this threshold. This is in very good agreement to experimentally observed oxygen evolution onsets. Due to the Sigmoid shape of the mobile concentration as a function of SOC without a defined onset, we assume a critical concentration of 11950 mol m^{-3} (23.6% state of lithiation) as the threshold for oxygen evolution, see

Ref. [40] (Supporting Information) for a more detailed discussion. The final rocksalt film thickness growth equation reads:

$$\frac{dL_{RS}}{dt} = \frac{V_{RS}\ D_{ox}}{L_{RS}\ \upsilon_{stoich}} \underbrace{c_{ox,lattice}\ \frac{\exp\left(\frac{-\Delta G(c_{Li})}{k_B T}\right)}{1+\exp\left(\frac{-\Delta G(c_{Li})}{k_B T}\right)}}_{c_{O_2,mob}} \tag{3}$$

with L_{RS} as the thickness of the rocksalt layer, V_{RS} as the molar volume of an assumed rocksalt phase, $c_{ox,lattice}$ as the available oxygen lattice concentration, D_{ox} as the diffusion coefficient of lattice oxygen in the growing phase and υ_{stoich} as a stoichiometric coefficient in the transformation reaction. To solve the growth equation, we initialize the layer thickness to 0.2 nm at all interfaces.

We take into account the rocksalt phase as a resistive film (RF). At interfaces between active material and electrolyte we model charge transfer via a kinetic Butler–Volmer current (Eq. (4)).

$$i_{BV} = 2\ i_0 \sinh\left(\frac{F}{2RT}(\Phi_s - \varphi_e - U_0(c_{if}) - R_{RS}\ i_{BV})\right) \tag{4}$$

The resistive term with $R_{RS} = \frac{L_{RS}}{\kappa_{RS}}$ in Eq. (4) describes the impact of film formation on Butler–Volmer kinetics. Intercalation kinetics thus depend on the solid electrical potential Φ_s, the electrochemical electrolyte potential φ_{el}, the open-circuit voltage U_0 and the resistive interface term. The prefactor i_0 depends on the exchange current density factor i_{00}, the concentration of Li ions in the electrolyte c_{el} as well as the maximum Li concentration in the solid active materials $c_{Li,max}$ as well as the solid phase concentration at the interface c_{if}.

$$i_0 = i_{00}\ c_{El}^{0.5}\ c_{if}^{0.5}\ (c_{Li,max} - c_{if})^{0.5} \tag{5}$$

To reduce computational complexity the interface concentration c_{if} is approximated according to:

$$c_{if} = c_{so} - \frac{i_{BV}\ L_{RS}}{F\ D_{Li,RS}} \tag{6}$$

c_{so} is the solid Li concentration next to the interface, F the Faraday constant and $D_{Li,RS}$ the diffusion coefficient of Li in the RS phase. Integration into our 3D framework allows us to observe the local phase transformation on the particle surface explicitly including the local environment in the electrolyte and electrode structure. Moreover, we have direct feedback between microscopic phase transformation and cell performance. The direct coupling between phase thickness and potential and concentration fields allows for more detailed predictions of local phase transformation compared to the P2D approach. Note that all simulations presented in this study have been performed using 3D-microstructure resolved simulations. Further details on the electrochemical models as well as the applied parameterization are given in the Supporting Information and in Ref. [40]. All simulations have been performed on the high-performance cluster JUSTUS2.

2.2. Structure segmentation

To study individual particles in the electrode, we apply a marker-based watershed algorithm to segment the full microstructure obtained from FIB-SEM tomography and highlight distinct particles in the electrode using the *scikit-image* [53] and *SciPy* [54] python packages. The watershed segmentation included a euclidean distance transform, a median filter on the obtained distances and a determination of significant minima. A marker-based watershed with connectivity 26 and without a watershed-line was applied. 20 particles with equivalent diameters between 3 µm and 17 µm spread across the electrode were chosen and will be tracked during cycling. Properties of the respective particles have been extracted using the *regionprops* function of the *scikit-image* package [53] and the equivalent diameter calculated as:

$$d_{equ} = \left(\frac{V_{part} \cdot 6}{\pi}\right)^{1/3} \tag{7}$$

The full workflow starting from the reconstruction of FIB-SEM images is outlined in Fig. 1.

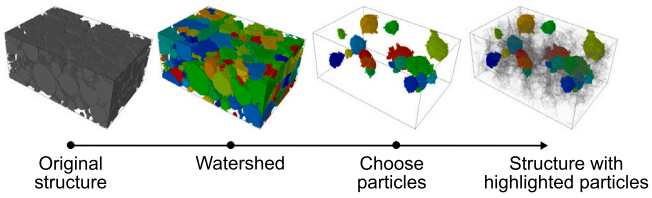

Fig. 1. FIB-SEM structure of the investigated electrode from Ref. [48] and the computational workflow applied for segmentation using a watershed algorithm. In the final structure, the highlighted particles are colored while the rest of the bulk active material is shaded gray.

3. Results and discussion

In this section, the simulation results for phase reconstruction are presented. We start with a discussion of the overall electrode degradation, followed by a detailed analysis of individual particles in the electrode. In the last section, we will discuss heterogeneity on single particles as a result of inhomogeneous lithiation.

3.1. Phase transformation on full electrode

To study the phase transformation in our virtual experiments we apply a charging protocol of a constant current (CC) charge (1C) from 3.6 V to 4.3 V with a subsequent constant voltage (CV) phase until a C/20 cutoff is reached [40]. A subsequent discharge is performed at a constant current of 1C. Fig. 2(a) shows the cell potential during cycling and the corresponding average rocksalt layer thickness of the reconstructed phase, which is denoted as the resistive film (RF). As shown in our previous work and in line with experiments, the reconstruction process starts to take place at around 4.3 V, i.e. once the concentration falls below a critical state of lithiation within the active material. The reconstructed layer thickness increases until the discharge starts and the concentration increases above the critical value. At the end of the CV phase, the average reconstructed thickness reaches approximately 0.4 nm and remains constant during subsequent discharge.

Our microstructure-resolved simulation provides spatially resolved information on the local formation of the reconstructed phase. The degradation model is based on the active material concentration (i.e., SOC) at interfaces between electrolyte and active material. Therefore, the evolution of active material lithium concentration directly impacts the rocksalt thickness on the material surface. To illustrate this, Fig. 2(b) shows the evolution of minimum concentration per electrode slice at snapshots 1–6 (indicated in (a)). We defined a critical concentration of 11950 mol m^{-3} (23.6% state of lithiation) below which the reconstruction process occurs (see our previous work for discussion [40]). This concentration is indicated by a horizontal dashed line. The slice-averaged film thickness at the same timesteps is also shown in Fig. 2(c). At the beginning of the CV phase, the concentration shows a strong gradient between separator and current collector. Upon further delithiation, the minimum concentration near the separator falls below the critical threshold and rocksalt formation starts to occur. This can be seen in a slight increase of the averaged film thickness near the separator. As a consequence, active material next to the separator is longer in a (more) delithiated state resulting in increased phase reconstruction. The inhomogeneous degradation continues until the minimum concentration of the whole electrode is below the critical concentration (t = 0.84 h). Beyond this point the reconstructed active material film starts to grow on the whole electrode, which is in line with previous predictions [39].

To understand the more pronounced delithiation at the separator, the Li-ion concentration in the electrolyte at the beginning of the CV phase is shown in Fig. 2(d) (initial concentration of 1 mol l^{-1}). The active material delithiation close to the separator is a consequence

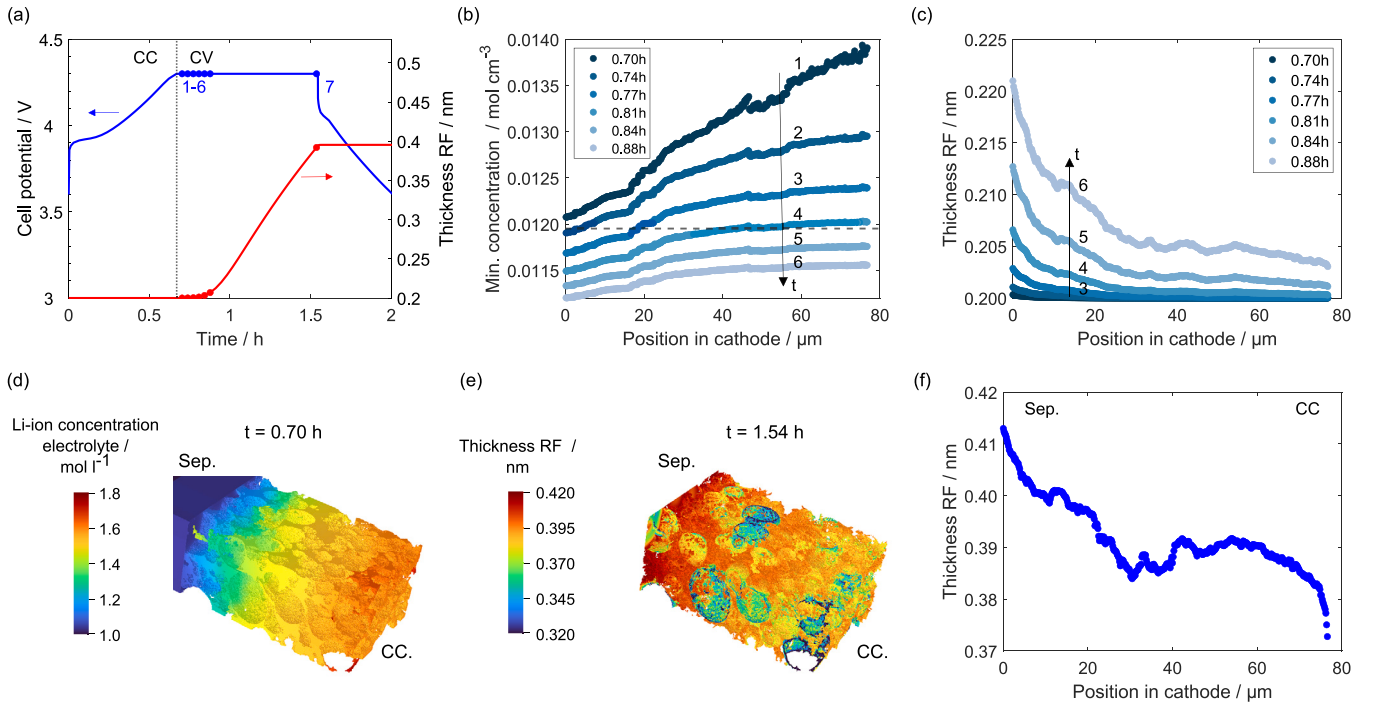

Fig. 2. (a) Voltage profile (left axis) and rocksalt thickness as the resistive film (RF) (right axis) during a 1C CCCV charge to 4.3 V. Snapshots at times 1–6 used in (b) are indicated for reference. The average thickness starts to increase once the critical SOC is reached. (b) Minimum concentration per slice for times indicated in (a) at the beginning of the CV phase. The critical concentration below which we assume active material degradation is indicated with a dashed line. The separator is located at 0. (c) The corresponding average rocksalt thickness for each slice in the electrode for times 1–6. (d) Distribution of Li-ion concentration in the electrolyte at the beginning of the CV phase (t = 0.7 h, timestep 1 in (a)). (e) Distribution of rocksalt layer thickness at the end of the CV phase (snapshot 7 in (a)) and corresponding slice-averaged layer thickness (f) over electrode through-direction. A gradient in resistive film thickness from separator to current collector is observed.

of insufficient ionic transport through the electrolyte phase at a high current density: Li ions near the current collector accumulate. This accumulation can be seen in Fig. 2(d). The ionic conductivity and the diffusion in the electrolyte decrease with increasing concentration [55], which hinders further transport of ions towards the anode. To show that indeed ionic transport leads to the inhomogeneous lithiation profile, we performed the same simulation with constant electrolyte parameters and an increased electrolyte diffusivity and conductivity. The resulting delithiation is much more homogeneous across the electrode, while the electrolyte concentration and electrochemical potential are also more homogeneous and exhibit a smaller gradient. The results are shown in Fig. S8 and Fig. S9 in the Supporting Information. A simulation, in which electronic transport limitations are negligible, resulted in the same delithiation pattern as our baseline simulation shown in Fig. 2. Therefore, electronic transport is not the limiting factor for delithiation, but the ionic transport that is too slow.

The final distribution of rocksalt thickness at the end of the CV phase (snapshot 7 in Fig. 2(a)) as well as the slice-averaged layer thickness over the electrode thickness are shown in Fig. 2(e) and (f), respectively. The maximum thickness can be found close to the separator due to the previously discussed heterogeneity in active material concentration. A decreasing film thickness towards the current collector with a thickness reduction of approximately 0.03 nm is observed. Overall, a strong gradient is present with a higher rocksalt thickness close to the separator and a smaller thickness near the current collector. Note that the overall difference in layer thicknesses is rather small. This is, however, in line with our previous predictions which showed similar gradients in the first cycle that accumulated over cycling to significant thicknesses [40]. Therefore, we interpret this to be an indication of how the growth process will continue upon further cycling or storage at high voltages.

Small peaks and low points like the minimum at approximately 30 µm can be attributed to the presence of very large particles in these slices with a very low reconstructed thickness that decrease the average value. Active material reconstruction on large particles is less pronounced, indicated by the blue color in the thickness profile in Fig. 2(e). This is due to a higher state of lithiation due to Li-ion diffusion and will be discussed in Section 3.2 in more detail. Note that our model only predicts rocksalt growth, while follow-up reactions with the electrolyte are not considered in this work. However, locally varying phase reconstruction also results in more local oxygen evolution. The oxygen can react with the organic solvents [3,10,56], which can lead to more detrimental side reactions and potentially an electrolyte dry-out. This could decrease intercalation locally even more and additionally promote inhomogeneities.

We also performed simulations at a lower current density (C/3) for charging and discharging with the same cutoff current for the CV phase as for 1C cycling. The final slice-averaged rocksalt thickness for both C-Rates is shown in Fig. 3(a). The overall rocksalt thickness is thinner for C/3 compared to 1C and the gradient is much less pronounced. We show the corresponding active material concentration gradient (minimum concentration) at the start of the phase reconstruction for C/3 cycling in Fig. 3(b). As expected, the concentration gradient at the beginning of the reconstruction process is much more homogeneous compared to the high current case, which also leads to a more uniform film thickness. The Li-ion distribution in the electrolyte within the 3D structure at the onset of rocksalt growth after CC charging is shown in the Supporting Information. The Li-ion concentration in the electrolyte is more homogeneously distributed across the electrode structure, opposed to the significant gradient that is present after 1C charging. At higher currents, ionic transport limitations become critical in the delithiation process as discussed earlier. Due to overall better active material utilization at low currents, the CV phase is shorter for C/3 cycling (0.44 h for C/3 and 0.88 h for 1C) which results in the overall thinner reconstructed layer. The dependency of the degradation

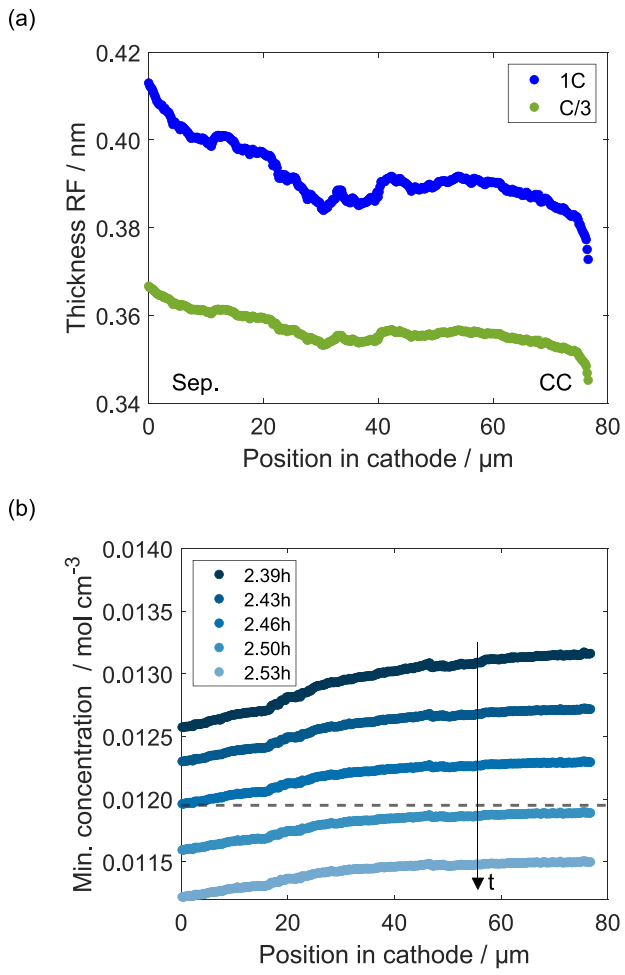

Fig. 3. (a) Slice-averaged film thickness after C/3 and 1C charging (CCCV). (b) Minimum concentration in electrode structure at the end of C/3 CC charging. The cycling data with indicated timesteps from (b) and the Li-ion concentration in the electrolyte at the end of CC charging are shown in the Supporting Information.

on the charging protocol thus needs to be considered in multivariate optimization.

3.2. Degradation of individual particles

Experimental single-particle studies on isolated particles revealed inhomogeneous lithiation and rocksalt growth [35]. However, individual particles are subject to a number of factors in real electrodes. Concentration and potential fields are influenced by the distribution of particle sizes and the carbon-binder-phase in addition to geometric properties like electrode thickness or tortuosity. To shed light on single-particle behavior in a full electrode, we can use our computational approach on the segmented structure (see Methods) to study the structural transformation process on individual particles in a realistic electrode setup.

In the following, we show the results of the same cycling protocol as used previously (1C CCCV charge, 1C discharge) and highlight the chosen particles.

Fig. 4(a) shows the increase in rocksalt thickness for the 20 particles highlighted in the inset. The particles with the minimum and the maximum detected rocksalt layer thickness are indicated in red and blue, respectively. The red and blue dashed lines are the upper and lower bound of the distribution of rocksalt layer thicknesses and all other particles are located in the shaded area in between. The global mean thickness for the electrode is shown for reference as well. The largest thickness can be attributed to particle R (15 in Supporting Information), which is a small particle next to the separator. The least reconstruction takes place on particle B (21 in Supporting Information), which is a large particle in the middle of the electrode. We will discuss the impact of their size and position below.

Fig. 4(b) shows the 3D visualization of the rocksalt thickness at the end of the CV phase, i.e. at 1.54 h. We observe an inhomogeneity across the particles that is mainly caused by their size and their position. Particles that are close to the separator show higher phase reconstruction, as seen by the higher rocksalt thickness compared to the region next to the current collector. This is in line with our previous discussion on the whole electrode structure. The effect of particle size is, however, also clearly visible. Large particles show less rocksalt formation, in line with the observation in Fig. 2(d). This is due to a higher Li concentration closer to the particle surface as a result of slow Li diffusion inside the particles, even at the end of the CV phase. As discussed in our previous work [40], large particles show less tendency for degradation since Li concentration falls below the critical threshold for phase reconstruction later compared to smaller particles. However, the slower equilibration dynamics in large particles determine and extend the CV phase additionally accelerating phase transformation on smaller particles. Indeed, the faradaic current density distribution at the end of CV phase still shows a significant current density on the surface of large particles (Fig. 4(c)). The current density on small particles, however, drops rapidly and is negligible at the end of the CV phase. Note that active material particles touch in the 3D structure resulting in locally zero or undefined rocksalt thickness and intercalation current. Therefore, some particles appear fractured on the images of rocksalt thickness and current density. Furthermore, we obtain individual particles from segmentation of a FIB-SEM tomography, which includes only secondary particles without internal porosity and additional crystallographic information on the primary particles. To assume the same interface model at all interfaces and only on the particle surface is thus a simplification. Additional aspects include crystal orientation in primary particles, as some crystal facets are more likely to deteriorate than others [57] as well as defects in the crystal structure or grain boundaries [58]. However, the transformation process is not fully understood on the atomistic scale and integrating all these aspects in a 3D-model is a very challenging task. We can, nonetheless, use the current model approach to predict general qualitative trends.

We now emphasized two important parameters that influence phase transformation process: the particle size and the particle position. To quantify both trends, we calculate the equivalent diameter of each of the highlighted particles and determine its centroid position as outlined in the Methods section. The average thickness of the reconstructed layer on each particle as function of its respective size is presented in Fig. 4(d). With increasing particle size the reconstructed thickness decreases and a linear trend can be seen. This is due to the extent of lithiation of particles with different size: Small particles delithiate faster as the diffusion length inside the particle is smaller. Larger particles take significantly longer to delithiate and thus extend the CV phase. Therefore, small particles effectively reach the critical lithium concentration faster and suffer from more degradation. The additional color mapping reveals a minor influence of the position as well: Particles near the current collector tend to have a thinner resistive film thickness as discussed in the previous section.

The dependence of the particle centroid position on rocksalt growth is shown in Fig. 4(e). The film thickness increases towards the separator, which reflects the overall delithiation behavior of the electrode as discussed earlier. However, the correlation is weaker compared to the linear trend observed for different particle size. That is, in part, due to the overlaying effect of particle size, which is revealed by the additional color map. Some outliers, like the points at 18 µm and 40 µm are caused by larger particles (very light color) that show less phase reconstruction.

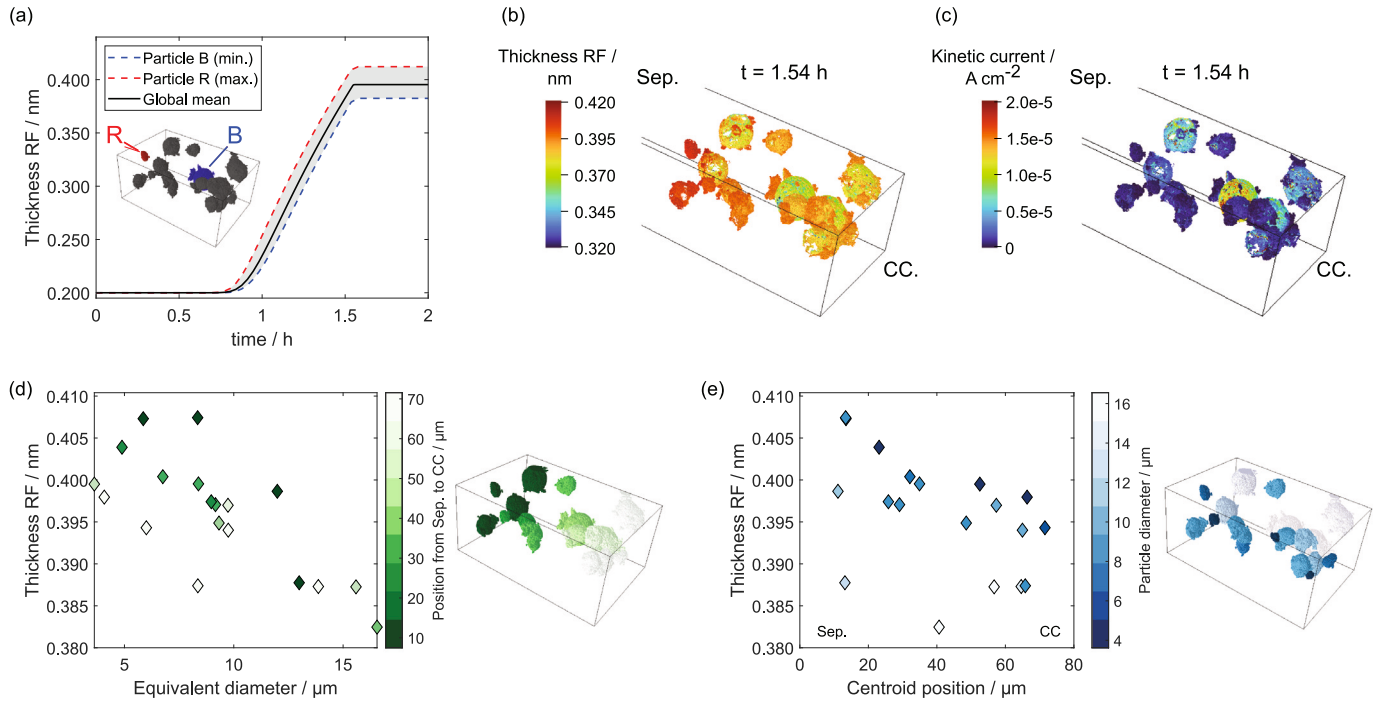

Fig. 4. (a) Growth of the reconstructed layer for the 20 individual particles and the global mean for reference. The smallest (dashed blue, particle B) and largest (dashed red, particle R) individual thickness evolution is indicated and the shaded region in between contains all other particles. The two particles B and R are also highlighted in the inset structure. (b) Reconstructed thickness and (c) Kinetic current density at the end of the CV phase for all 20 particles. Dependence of rocksalt thickness (d) on equivalent particle diameter and (e) on centroid position of the particle. Colors indicate the particle positions and sizes, which are also used in the electrode structures for better visualization.

While experimental validation for our predictions is difficult to obtain, a recent nano X-ray CT study by Goldbach et al. [26] found a more pronounced degradation due to particle cracking at the separator-facing side of the electrode as well as more particle cracking for small to medium-sized particles, which they attributed to an inhomogeneous lithiation. Assuming the degradation phenomena result from the same origin, their findings support our model predictions of a higher degradation at the separator due to transport limitations in the electrolyte as well as higher degradation of small particles due to a higher surface-to-volume ratio and shorter diffusion length scales.

Our particle-by-particle analysis reveals the role of particle size and position in the electrode and can thus inform cathode design strategies.

3.3. Inhomogeneity on the particle scale

Another important aspect is the inhomogeneity across individual particles that has been observed experimentally [35]. Through our microstructure-resolved simulation, we inherently observe the direct correlation between Li concentration in the active material and rocksalt growth and, vice versa, the impact of an inhomogeneous rocksalt layer on lithiation dynamics. Fig. 5 shows the rocksalt thicknesses and concentration profiles of particle R, which is close to the separator (highlighted in Fig. 4(a)). Similar to the electrode scale we observe heterogeneous film growth on single particles, too. The color coding indicates the relative deviation from the respective average value, which is indicated below each image. The corresponding plot with absolute values is shown in the Supporting Information. The snapshots are taken at the beginning of the CV phase, in the middle of the CV phase and at its end right before the cutoff current is reached. The view on the particle is from the side, i.e the separator is located on the left and the current collector on the right hand side of the particle. For a full view and information on its position in the electrode, the reader is referred to the Supporting Information.

At the beginning of the CV phase (Fig. 5(a)), the film thickness is homogeneously distributed (0.2 nm initial thickness), which is reflected by the uniform shading. During the CV phase, the rocksalt thickness starts to increase all over the particle with a more pronounced growth on the separator-facing side of the particle. At t = 1.12 h, the left side of the particle deviates from the average thickness by approximately 1.6%. At the end of the CV phase, a gradient persists, but is slightly less pronounced with 1% deviation. To understand the reason for this heterogeneity, we study the concentration profiles at the same time steps, shown in Fig. 5(b). The Li ion concentration in the active material reveals an inhomogeneity in concentration at the end of CC charging (t = 0.7 h) with a higher degree of delithiation on the left side than on the right side of the particle. The strong deviation of −6% from the average value is due to the particle interior, which is still at a higher state of lithiation than the visible surface at the beginning of the CV phase. The very inhomogeneous delithiation causes inhomogeneous rocksalt growth as the more delithiated surfaces are exposed to a critical state-of-lithiation earlier. The separator-facing (left) side of the particle, which has a lower concentration, therefore shows more reconstruction. During the CV phase, the concentration gradient minimizes until reaching a homogeneous state of lithiation at the end of the CV phase. While the concentration equilibrates during the CV phase, the inhomogeneous formation of rocksalt layer is irreversible. The impact on subsequent cycling is investigated in Fig. 6. While we emphasized the impact of particle size and position, the particle shape influences the lithiation pattern due to locally varying overpotentials [59]. This effect is inherently included in our modeling approach as we investigate particles in a realistic electrode. Fig. 6 shows the lithium concentration in the particle after a subsequent 1C discharge for a case with degradation and a reference case without any degradation. The relative deviation from the average value (indicated below each image) is shown here; the absolute concentration values are shown in the Supporting Information. Simulations including the phase transformation show a more inhomogeneous Li distribution at

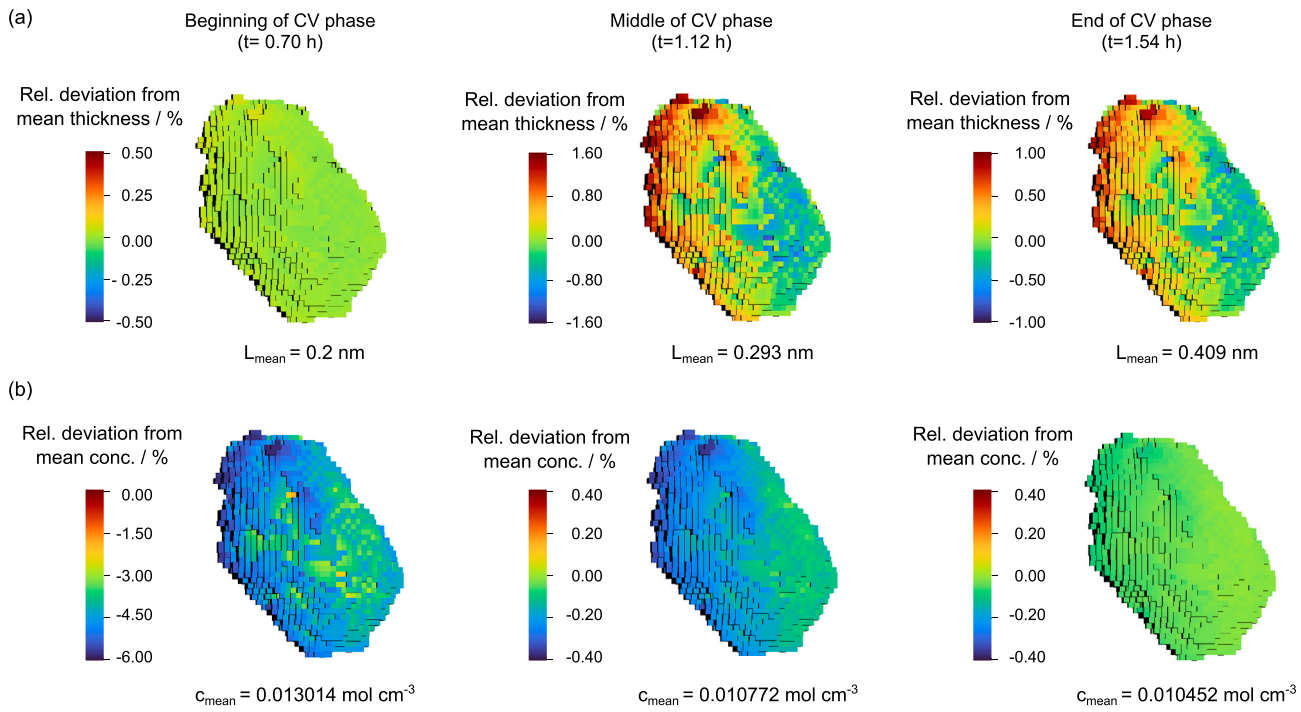

Fig. 5. (a) Reconstructed thickness profiles and (b) concentration profiles for particle R at the beginning of the CV phase (t = 0.70 h), the middle of the CV phase (t = 1.12 h) and the end of the CV phase (t = 1.54 h). All plots show the relative deviation from the mean values calculated for the whole particle, which are indicated below the respective image. The left side of the particle faces the separator and the right side the current collector. See Fig. 4(a) and Fig. S2 for more detail on its position.

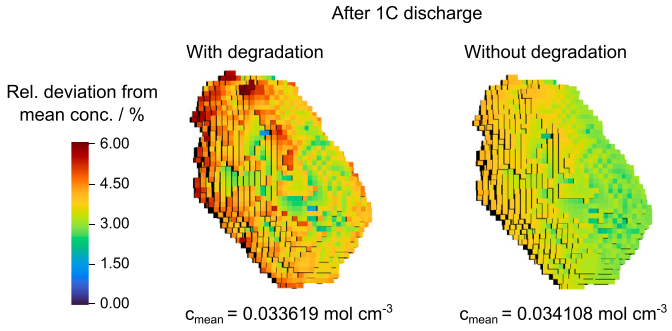

Fig. 6. Concentration profiles of single particle after subsequent 1C discharge with resistive film model (a) and without degradation (b). Shown is the deviation from the average particle concentration, which is indicated below the particle. Without degradation, the state of lithiation is much more homogeneous.

the end of discharge compared to the same simulation without any degradation. Additionally, the average Li concentration at the end of discharge including degradation is 1.4% lower compared to the pristine case. This highlights the impact of additional overpotentials due to the resistive layers on cell performance. The large deviations from the average concentration result from the particle interior, which is not homogeneously delithiated after a CC (dis-)charging step. While the overall inhomogeneity in predicted rocksalt thickness is not very large, we observe a noticeable impact on lithiation. Expecting an increasing inhomogeneity over cycling as discussed above and predicted in our previous study [40] also increasing sensitivity of the lithiation can be expected.

In summary, we show how inhomogeneous lithiation, induced by the complex concentration and potential fields in an electrode, can lead to inhomogeneous aging and, vice versa, how inhomogeneous aging can lead to inhomogeneous lithiation. In real world operation, this will most likely be in addition to other influencing factors such as crystal orientation and prevailing surface terminations. Regarding electrode design, particle position and size effects need to be taken into account when considering degradation phenomena in electrode materials.

4. Conclusions

Using 3D microstructure-resolved simulation on a realistic, high-energy NMC811 electrode, we investigate spatially resolved phase reconstruction of the layered material to a rocksalt phase. We show an inhomogeneous degradation across the electrode with a higher active material degradation at the separator and a smaller degradation at the current collector. A watershed segmentation of the structure allows us to observe individual particles during delithiation and monitor phase reconstruction on these particles. We show a high correlation between the reconstructed film thickness and both the position as well as the particle size due to their delithiation behavior. Experimentally, inhomogeneous rocksalt growth has been demonstrated [20,35]. Our 3D microstructure-resolved simulations offer an explanation for the reported inhomogeneity on particles: the degree of delithiation is not necessarily homogeneously distributed at the particle surface, depending on factors like its position or its shape. To the authors knowledge, this is the first simulation of rocksalt formation on a realistic electrode structure. It therefore presents novel insights into relations between particle size, position and indirectly shape that are experimentally hardly accessible. Future development should therefore aim to take into account design parameters like particle size distribution when studying degradation of cathode active materials by specifically designing experiments to balance the advantages and disadvantages of different particle size distributions on the cycling performance and material degradation. Strategies to mitigate oxygen loss and phase transformation include doping or surface coatings. Future research should therefore investigate their effectiveness in providing a homogeneous protection of individual particles in full electrodes.

Our results emphasize the need for multiscale simulations of lithium-ion battery degradation. While general trends can be predicted very well with homogenized P2D models, important structural aspects such as inhomogeneity in particles can only be directly observed in structure-resolved simulations. This helps to deepen the understanding of degradation processes in order to develop mitigation strategies through material, electrode and cell design.

CRediT authorship contribution statement

Svenja Both: Writing – original draft, Visualization, Formal analysis, Data curation, Conceptualization. **Simon Hein:** Writing – review & editing, Software. **Arnulf Latz:** Writing – review & editing, Funding acquisition. **Timo Danner:** Writing – review & editing, Supervision, Funding acquisition.

Declaration of competing interest

The authors declare that they have no known competing financial interests or personal relationships that could have appeared to influence the work reported in this paper.

Acknowledgments

The authors thankfully acknowledge funding by the German federal ministry of education and research through the project “MiCha”, Germany (03XP0317D) and by the German Research Foundation (DFG) within the research training group SiMET, Germany under project number 281041241/GRK2218. The authors acknowledge support from the state of Baden-Württemberg through bwHPC and the German Research Foundation (DFG), Germany through grant no INST 40/575-1 FUGG (JUSTUS 2 cluster). This work contributes to the research performed at CELEST (Center for Electrochemical Energy Storage Ulm-Karlsruhe), Germany.

Appendix A. Supplementary data

Supplementary material related to this article can be found online at https://doi.org/10.1016/j.ensm.2026.104994.

Data availability

Data will be made available on request.

References

[1] W. Li, E.M. Erickson, A. Manthiram, High-nickel layered oxide cathodes for lithium-based automotive batteries, Nat. Energy 5 (1) (2020) 26–34, http://dx.doi.org/10.1038/s41560-019-0513-0.

[2] S. Oswald, H.A. Gasteiger, The structural stability limit of layered lithium transition metal oxides due to oxygen release at high state of charge and its dependence on the nickel content, J. Electrochem. Soc. 170 (3) (2023) 030506, http://dx.doi.org/10.1149/1945-7111/acbf80.

[3] R. Jung, M. Metzger, F. Maglia, C. Stinner, H.A. Gasteiger, Oxygen release and its effect on the cycling stability of LiNi x Mn y Co z O 2 (NMC) cathode materials for Li-ion batteries, J. Electrochem. Soc. 164 (7) (2017) A1361–A1377, http://dx.doi.org/10.1149/2.0021707jes.

[4] C. Xu, K. Märker, J. Lee, A. Mahadevegowda, P.J. Reeves, S.J. Day, M.F. Groh, S.P. Emge, C. Ducati, B. Layla Mehdi, C.C. Tang, C.P. Grey, Bulk fatigue induced by surface reconstruction in layered Ni -rich cathodes for Li-ion batteries, Nat. Mater. 20 (1) (2021) 84–92, http://dx.doi.org/10.1038/s41563-020-0767-8.

[5] F. Lin, I.M. Markus, D. Nordlund, T.-C. Weng, M.D. Asta, H.L. Xin, M.M. Doeff, Surface reconstruction and chemical evolution of stoichiometric layered cathode materials for lithium-ion batteries, Nat. Commun. 5 (1) (2014) 3529, http://dx.doi.org/10.1038/ncomms4529.

[6] H. Zhang, H. Liu, L.F.J. Piper, M.S. Whittingham, G. Zhou, Oxygen loss in layered oxide cathodes for Li-ion batteries: mechanisms, effects, and mitigation, Chem. Rev. 122 (6) (2022) 5641–5681, http://dx.doi.org/10.1021/acs.chemrev.1c00327.

[7] N.A. Shah, G.J. Páez Fajardo, H. Banerjee, G.C. Pandey, A.S. Menon, M. Ans, V. Majherova, G. Bree, S. Bolloju, D.C. Grinter, P. Ferrer, P.K. Thakur, T.-L. Lee, M.J. Loveridge, A.J. Morris, C.P. Grey, L.F.J. Piper, Nature of the oxygen -loss-induced rocksalt layer and its impact on capacity fade in Ni-rich layered oxide cathodes, ACS Energy Lett. 10 (3) (2025) 1313–1320, http://dx.doi.org/10.1021/acsenergylett.5c00324.

[8] Q. Xie, Z. Cui, A. Manthiram, Unveiling the stabilities of nickel-based layered oxide cathodes at an identical degree of delithiation in lithium-based batteries, Adv. Mater. 33 (32) (2021) 2100804, http://dx.doi.org/10.1002/adma.202100804.

[9] F. Friedrich, B. Strehle, A.T.S. Freiberg, K. Kleiner, S.J. Day, C. Erk, M. Piana, H.A. Gasteiger, Editors’ choice —capacity fading mechanisms of NCM-811 cathodes in lithium-ion batteries studied by X-ray diffraction and other diagnostics, J. Electrochem. Soc. 166 (15) (2019) A3760–A3774, http://dx.doi.org/10.1149/2.0821915jes.

[10] R. Jung, M. Metzger, F. Maglia, C. Stinner, H.A. Gasteiger, Chemical versus electrochemical electrolyte oxidation on NMC111, NMC622, NMC811, LNMO, and conductive carbon, J. Phys. Chem. Lett. 8 (19) (2017) 4820–4825, http://dx.doi.org/10.1021/acs.jpclett.7b01927.

[11] L. Hartmann, L. Reuter, L. Wallisch, A. Beiersdorfer, A. Adam, D. Goldbach, T. Teufl, P. Lamp, H.A. Gasteiger, J. Wandt, Depletion of electrolyte salt upon calendaric aging of lithium-ion batteries and its effect on cell performance, J. Electrochem. Soc. 171 (6) (2024) 060506, http://dx.doi.org/10.1149/1945-7111/ad4821.

[12] J. Wandt, A.T. Freiberg, A. Ogrodnik, H.A. Gasteiger, Singlet oxygen evolution from layered transition metal oxide cathode materials and its implications for lithium-ion batteries, Mater. Today 21 (8) (2018) 825–833, http://dx.doi.org/10.1016/j.mattod.2018.03.037.

[13] W.M. Dose, I. Temprano, J.P. Allen, E. Björklund, C.A. O’Keefe, W. Li, B.L. Mehdi, R.S. Weatherup, M.F.L. De Volder, C.P. Grey, Electrolyte reactivity at the charged Ni-rich cathode interface and degradation in Li-ion batteries, ACS Appl. Mater. Interfaces 14 (11) (2022) 13206–13222, http://dx.doi.org/10.1021/acsami.1c22812.

[14] H. Zheng, S. Peng, S. Liang, W. Yang, C. Chen, C. Wang, R. Yu, Progress and challenges of Ni-rich layered cathodes for all-solid-state lithium batteries, Adv. Funct. Mater. 35 (16) (2025) 2418274, http://dx.doi.org/10.1002/adfm.202418274.

[15] R.A. House, U. Maitra, L. Jin, J.G. Lozano, J.W. Somerville, N.H. Rees, A.J. Naylor, L.C. Duda, F. Massel, A.V. Chadwick, S. Ramos, D.M. Pickup, D.E. McNally, X. Lu, T. Schmitt, M.R. Roberts, P.G. Bruce, What triggers oxygen loss in oxygen redox cathode materials? Chem. Mater. 31 (9) (2019) 3293–3300, http://dx.doi.org/10.1021/acs.chemmater.9b00227.

[16] A. Massaro, A.B. Muñoz-García, P.P. Prosini, C. Gerbaldi, M. Pavone, Unveiling oxygen redox activity in P2-type Na_x $Ni_{0.25}$ $Mn_{0.68}$ O_2 high-energy cathode for Na-ion batteries, ACS Energy Lett. 6 (7) (2021) 2470–2480, http://dx.doi.org/10.1021/acsenergylett.1c01020.

[17] Y. Chu, Y. Mu, L. Zou, F. Wu, L. Yang, Y. Feng, L. Zeng, Oxygen release in Ni-rich layered cathode for lithium-ion batteries: Mechanisms and mitigating strategies, ChemElectroChem 11 (14) (2024) e202300653, http://dx.doi.org/10.1002/celc.202300653.

[18] C. Yang, Y. Li, W. Su, X. Zhu, L. Hao, X. Wang, S. Wu, L. Chen, D. Cao, Y. Su, N. Li, F. Wu, Aluminium doping in single-crystal nickel-rich cathodes: insights into electrochemical degradation and enhancement, J. Mater. Chem. A 12 (32) (2024) 20910–20920, http://dx.doi.org/10.1039/D4TA02355B.

[19] J. Xu, W.-L. Wong, H. Du, Y. Kang, Y. Zhao, B. Lan, Z. Guo, M.-M. Titirici, F. Kang, B. Li, Upcycling the cathodes of spent lithium ion batteries into high-performance cathodes, Nano Res. Energy 4 (3) (2025) e9120174, http://dx.doi.org/10.26599/NRE.2025.9120174.

[20] K. Vettori, S. Schröder, L. Ahrens, R. Wilhelm, S. Kremer, J.K. Eckhardt, T. Brezesinski, A. Kondrakov, J. Mayer, A. Henss, J. Janek, Chemical and structural degradation of single crystalline high-nickel cathode materials during high-voltage holds, Adv. Energy Mater. 15 (33) (2025) 2502148, http://dx.doi.org/10.1002/aenm.202502148.

[21] D. Li, H. Li, D. Danilov, L. Gao, J. Zhou, R.-A. Eichel, Y. Yang, P.H. Notten, Temperature-dependent cycling performance and ageing mechanisms of C6/LiNi1/3Mn1/3Co1/3O2 batteries, J. Power Sources 396 (2018) 444–452, http://dx.doi.org/10.1016/j.jpowsour.2018.06.035.

[22] E. Björklund, C. Xu, W.M. Dose, C.G. Sole, P.K. Thakur, T.-L. Lee, M.F.L. De Volder, C.P. Grey, R.S. Weatherup, Cycle-induced interfacial degradation and transition-metal cross-over in $LiNi_{0.8}$ $Mn_{0.1}$ $Co_{0.1}$ O_2 –graphite cells, Chem. Mater. 34 (5) (2022) 2034–2048, http://dx.doi.org/10.1021/acs.chemmater.1c02722.

[23] Z. Ruff, C. Xu, C.P. Grey, Transition metal dissolution and degradation in nmc811-graphite electrochemical cells, J. Electrochem. Soc. 168 (6) (2021) 060518, http://dx.doi.org/10.1149/1945-7111/ac0359.

[24] J. Wandt, A. Freiberg, R. Thomas, Y. Gorlin, A. Siebel, R. Jung, H.A. Gasteiger, M. Tromp, Transition metal dissolution and deposition in Li -ion batteries investigated by operando X-ray absorption spectroscopy, J. Mater. Chem. A 4 (47) (2016) 18300–18305, http://dx.doi.org/10.1039/C6TA08865A.

[25] S. Solchenbach, G. Hong, A.T.S. Freiberg, R. Jung, H.A. Gasteiger, Electrolyte and SEI decomposition reactions of transition metal ions investigated by on-line electrochemical mass spectrometry, J. Electrochem. Soc. 165 (14) (2018) A3304–A3312, http://dx.doi.org/10.1149/2.0511814jes.

[26] D. Goldbach, J. Gluch, T. Graf, M. Gaus, S. Käbitz, M. Zillmer, U. Krewer, An efficient approach for quantifying the mechanical degradation of Ni-rich NMC-based cathodes for lithium-ion batteries using nano-XCT analysis, ChemElectroChem 10 (20) (2023) e202300353, http://dx.doi.org/10.1002/celc.202300353.

[27] J.K. Morzy, W.M. Dose, P.E. Vullum, M.C. Lai, A. Mahadevegowda, M.F.L. De Volder, C. Ducati, Origins and importance of intragranular cracking in layered lithium transition metal oxide cathodes, ACS Appl. Energy Mater. 7 (9) (2024) 3945–3956, http://dx.doi.org/10.1021/acsaem.4c00279.

[28] S. Lee, L. Su, A. Mesnier, Z. Cui, A. Manthiram, Cracking vs. surface reactivity in high-nickel cathodes for lithium-ion batteries, Joule 7 (11) (2023) 2430–2444, http://dx.doi.org/10.1016/j.joule.2023.09.006.

[29] Y.-Y. Wang, X.-Q. Zhang, M.-Y. Zhou, J.-Q. Huang, Mechanism, quantitative characterization, and inhibition of corrosion in lithium batteries, Nano Res. Energy 2 (2023) e9120046, http://dx.doi.org/10.26599/NRE.2023.9120046.

[30] R. Jung, F. Linsenmann, R. Thomas, J. Wandt, S. Solchenbach, F. Maglia, C. Stinner, M. Tromp, H.A. Gasteiger, Nickel, manganese, and cobalt dissolution from Ni-rich NMC and their effects on NMC622-graphite cells, J. Electrochem. Soc. 166 (2) (2019) A378–A389, http://dx.doi.org/10.1149/2.1151902jes.

[31] S. Jung, H. Gwon, J. Hong, K. Park, D. Seo, H. Kim, J. Hyun, W. Yang, K. Kang, Understanding the degradation mechanisms of LiNi 0.5 Co 0.2 Mn 0.3 O 2 cathode material in lithium ion batteries, Adv. Energy Mater. 4 (1) (2014) 1300787, http://dx.doi.org/10.1002/aenm.201300787.

[32] H. Ryu, G. Park, C.S. Yoon, Y. Sun, Microstructural degradation of Ni-rich Li[Ni $_x$ Co $_y$ Mn$_{1-x-y}$]O$_2$ cathodes during accelerated calendar aging, Small 14 (45) (2018) 1803179, http://dx.doi.org/10.1002/smll.201803179.

[33] C. Misiewicz, R. Lundström, I. Ahmed, M.J. Lacey, W.R. Brant, E.J. Berg, Online electrochemical mass spectrometry on large-format Li -ion cells, J. Power Sources 554 (2023) 232318, http://dx.doi.org/10.1016/j.jpowsour.2022.232318.

[34] A.T.S. Freiberg, S. Qian, J. Wandt, H.A. Gasteiger, E.J. Crumlin, Surface oxygen depletion of layered transition metal oxides in Li-ion batteries studied by operando ambient pressure X-ray photoelectron spectroscopy, ACS Appl. Mater. Interfaces 15 (3) (2023) 4743–4754, http://dx.doi.org/10.1021/acsami.2c19008.

[35] Z. Lun, A.J. Merryweather, A. Mahadevegowda, S.S. Pandurangi, C. Xu, S. Fairclough, V.S. Deshpande, N.A. Fleck, C. Ducati, C. Schnedermann, A. Rao, C.P. Grey, Operando single-particle imaging reveals that asymmetric ion flux contributes to capacity degradation in aged Ni-rich layered cathodes, Energy Environ. Sci. 18 (9) (2025) 4097–4107, http://dx.doi.org/10.1039/D5EE00267B.

[36] S. Both, A.D. Poletayev, T. Danner, A. Latz, M.S. Islam, Probing surface degradation pathways of charged nickel-oxide cathode materials using machine-learning interatomic potentials, ACS Appl. Mater. Interfaces 17 (40) (2025) 56612–56620, http://dx.doi.org/10.1021/acsami.5c11818.

[37] A.R. Genreith-Schriever, H. Banerjee, A.S. Menon, E.N. Bassey, L.F. Piper, C.P. Grey, A.J. Morris, Oxygen hole formation controls stability in LiNiO2 cathodes, Joule 7 (7) (2023) 1623–1640, http://dx.doi.org/10.1016/j.joule.2023.06.017.

[38] F. Kong, C. Liang, L. Wang, Y. Zheng, S. Perananthan, R.C. Longo, J.P. Ferraris, M. Kim, K. Cho, Kinetic stability of bulk LiNiO 2 and surface degradation by oxygen evolution in LiNiO 2 –based cathode materials, Adv. Energy Mater. 9 (2) (2019) 1802586, http://dx.doi.org/10.1002/aenm.201802586.

[39] M. Zhuo, G. Offer, M. Marinescu, Degradation model of high-nickel positive electrodes: Effects of loss of active material and cyclable lithium on capacity fade, J. Power Sources 556 (36) (2023) 232461, http://dx.doi.org/10.1016/j.jpowsour.2022.232461.

[40] S. Both, S. Hein, T. Danner, A. Latz, Modeling oxygen loss and phase transformation in Ni-rich cathode materials: Impact of electrode microstructure, Batter. Supercaps 8 (8) (2025) e202400802, http://dx.doi.org/10.1002/batt.202400802.

[41] A. Ghosh, J.M. Foster, G. Offer, M. Marinescu, A shrinking-core model for the degradation of high-nickel cathodes (NMC811) in Li-ion batteries: Passivation layer growth and oxygen evolution, J. Electrochem. Soc. 168 (2) (2021) 020509, http://dx.doi.org/10.1149/1945-7111/abdc71.

[42] R. Xu, Y. Yang, F. Yin, P. Liu, P. Cloetens, Y. Liu, F. Lin, K. Zhao, Heterogeneous damage in Li -ion batteries: Experimental analysis and theoretical modeling, J. Mech. Phys. Solids 129 (2019) 160–183, http://dx.doi.org/10.1016/j.jmps.2019.05.003.

[43] A.M. Boyce, E. Martínez-Pañeda, A. Wade, Y.S. Zhang, J.J. Bailey, T.M. Heenan, D.J. Brett, P.R. Shearing, Cracking predictions of lithium-ion battery electrodes by X -ray computed tomography and modelling, J. Power Sources 526 (2022) 231119, http://dx.doi.org/10.1016/j.jpowsour.2022.231119.

[44] F.L.E. Usseglio-Viretta, A.M. Colclasure, J. Allen, P.J. Weddle, D.P. Finegan, P. Graf, K. Smith, Microstructure scale lithium-ion battery modeling: Part II. On in-plane heterogeneities and the mechanisms that regulate them, J. Electrochem. Soc. 172 (9) (2025) 090527, http://dx.doi.org/10.1149/1945-7111/ae04a2.

[45] F.L.E. Usseglio-Viretta, A.M. Colclasure, J. Allen, P.J. Weddle, D.P. Finegan, P. Graf, K. Smith, Microstructure scale lithium-ion battery modeling: Part I. On through-plane heterogeneity, impact of mesh representation, title=and differences between macro- and microscale models, J. Electrochem. Soc. 172 (8) (2025) 080508, http://dx.doi.org/10.1149/1945-7111/adf35d.

[46] L.J. Bolay, T. Schmitt, S. Hein, O.S. Mendoza-Hernandez, E. Hosono, D. Asakura, K. Kinoshita, H. Matsuda, M. Umeda, Y. Sone, A. Latz, B. Horstmann, Microstructure-resolved degradation simulation of lithium-ion batteries in space applications, J. Power Sources Adv. 14 (2022) 100083, http://dx.doi.org/10.1016/j.powera.2022.100083.

[47] F.L.E. Usseglio-Viretta, A.M. Colclasure, J. Allen, P.J. Weddle, D.P. Finegan, P. Graf, K. Smith, Microstructure scale lithium-ion battery modeling: Part III. When and where lithium plating occurs and its correlation with the electrode microstructure, J. Electrochem. Soc. 172 (9) (2025) 090502, http://dx.doi.org/10.1149/1945-7111/adfca0.

[48] A. Lindner, S. Both, W. Menesklou, S. Hein, T. Danner, A. Latz, U. Krewer, Analyzing and improving conductive networks in commercial high-energy Ni-rich cathodes, Batter. Supercaps 7 (12) (2024) e202400503, http://dx.doi.org/10.1002/batt.202400503.

[49] W.T. John Newman, Porous–electrode theory with battery applications, AiChe J. 21 (1) (1975) 25–41, http://dx.doi.org/10.1002/aic.690210103.

[50] A. Latz, J. Zausch, Thermodynamic consistent transport theory of Li-ion batteries, J. Power Sources 196 (6) (2011) 3296–3302, http://dx.doi.org/10.1016/j.jpowsour.2010.11.088.

[51] T. Danner, M. Singh, S. Hein, J. Kaiser, H. Hahn, A. Latz, Thick electrodes for Li -ion batteries: A model based analysis, J. Power Sources 334 (2016) 191–201, http://dx.doi.org/10.1016/j.jpowsour.2016.09.143.

[52] S. Hein, T. Danner, D. Westhoff, B. Prifling, R. Scurtu, L. Kremer, A. Hoffmann, A. Hilger, M. Osenberg, I. Manke, M. Wohlfahrt-Mehrens, V. Schmidt, A. Latz, Influence of conductive additives and binder on the impedance of lithium-ion battery electrodes: effect of morphology, J. Electrochem. Soc. 167 (1) (2020) 013546, http://dx.doi.org/10.1149/1945-7111/ab6b1d.

[53] S. Van Der Walt, J.L. Schönberger, J. Nunez-Iglesias, F. Boulogne, J.D. Warner, N. Yager, E. Gouillart, T. Yu, scikit-image: image processing in Python, PeerJ 2 (2014) e453, http://dx.doi.org/10.7717/peerj.453.

[54] P. Virtanen, R. Gommers, T.E. Oliphant, M. Haberland, T. Reddy, D. Cournapeau et al., SciPy 1.0: fundamental algorithms for scientific computing in Python, Nature Methods 17 (3) (2020) 261–272, http://dx.doi.org/10.1038/s41592-019-0686-2.

[55] J. Landesfeind, H.A. Gasteiger, Temperature and concentration dependence of the ionic transport properties of lithium-ion battery electrolytes, J. Electrochem. Soc. 166 (14) (2019) A3079–A3097, http://dx.doi.org/10.1149/2.0571912jes.

[56] B.L.D. Rinkel, D.S. Hall, I. Temprano, C.P. Grey, Electrolyte oxidation pathways in lithium-ion batteries, J. Am. Chem. Soc. 142 (35) (2020) 15058–15074, http://dx.doi.org/10.1021/jacs.0c06363.

[57] M. Kim, L. Zou, S.-B. Son, I.D. Bloom, C. Wang, G. Chen, Improving LiNiO2 cathode performance through particle design and optimization, J. Mater. Chem. A 10 (24) (2022) 12890–12899, http://dx.doi.org/10.1039/D2TA02492F.

[58] A.G. Squires, L. Ganeshkumar, C.N. Savory, S.R. Kavanagh, D.O. Scanlon, Oxygen dimerization as a defect-driven process in bulk $LiNiO_2$, ACS Energy Lett. 9 (8) (2024) 4180–4187, http://dx.doi.org/10.1021/acsenergylett.4c01307.

[59] I. Traskunov, A. Latz, Localized fluctuations of electrochemical properties in porous electrodes of lithium-ion batteries: Beyond porous electrode theory, Electrochim. Acta 379 (2021) 138144, http://dx.doi.org/10.1016/j.electacta.2021.138144.